A Simple Multicloud Parameterization for Convectively Coupled Tropical Waves. Part II: Nonlinear Simulations

BOUALEM KHOUIDER

Department of Mathematics and Statistics, University of Victoria, Victoria, British Columbia, Canada

ANDREW J. MAJDA

Department of Mathematics, and Center for Atmosphere Ocean Science, Courant Institute, New York University, New York, New York

(Manuscript received 11 July 2005, in final form 9 February 2006)

ABSTRACT

Observations in the Tropics point to the important role of three cloud types, congestus, stratiform, and deep convective clouds, besides ubiquitous shallow boundary layer clouds for both the climatology and large-scale organized anomalies such as convectively coupled Kelvin waves, two-day waves, and the Madden–Julian oscillation. Recently, the authors have developed a systematic model convective parameterization highlighting the dynamic role of the three cloud types through two baroclinic modes of vertical structure: a deep convective heating mode and a second mode with lower troposphere heating and cooling corresponding respectively to congestus and stratiform clouds. The model includes both a systematic moisture equation where the lower troposphere moisture increases through detrainment of shallow cumulus clouds, evaporation of stratiform rain, and moisture convergence and decreases through deep convective precipitation and also a nonlinear switch that favors either deep or congestus convection depending on whether the lower middle troposphere is moist or dry. Here these model convective parameterizations are applied to a 40 000-km periodic equatorial ring without rotation, with a background sea surface temperature (SST) gradient and realistic radiative cooling mimicking a tropical warm pool. Both the emerging "Walker cell" climatology and the convectively coupled wave fluctuations are analyzed here while various parameters in the model are varied. The model exhibits weak congestus moisture coupled waves outside the warm pool in a turbulent bath that intermittently amplify in the warm pool generating convectively coupled moist gravity wave trains propagating at speeds ranging from 15 to 20 m s^{-1} over the warm pool, while retaining a classical Walker cell in the mean climatology. The envelope of the deep convective events in these convectively coupled wave trains often exhibits large-scale organization with a slower propagation speed of 3–5 m s^{-1} over the warm pool and adjacent region. Occasional much rarer intermittent deep convection also occurs outside the warm pool. The realistic parameter regimes in the multicloud model are identified as those with linearized growth rates for large scale instabilities roughly in the range of 0.5 K day^{-1}.

1. Introduction

Observational data indicate that tropical convection is organized on a hierarchy of scales ranging from hundreds of kilometers due to organized mesoscale complexes to equatorial synoptic scales of order a thousand kilometers with convectively coupled superclusters to intraseasonal oscillations over the planetary scales of order 40 000 km (Nakazawa 1988; Wheeler and Kiladis 1999; Wheeler et al. 2000). Recent analysis of observations over the warm pool in the Tropics reveals the ubiquity of three cloud types above the boundary layer: shallow/congestus clouds, stratiform clouds, and deep penetrative cumulus clouds (Lin and Johnson 1996; Johnson et al. 1999). Furthermore, recent analysis of observed convectively coupled waves on the large scales reveals a similar multicloud convective structure with leading congestus cloud decks that moisten and precondition the lower troposphere followed by deep convection and finally trailing decks of stratiform precipitation; this structure applies to the eastward-propagating convectively coupled Kelvin waves (Wheeler and Kiladis 1999; Straub and Kiladis 2002) and westward-propagating two-day waves (Haertel and Kiladis 2004), which reside on equatorial synoptic

Corresponding author address: Dr. Boualem Khouider, Mathematics and Statistics, University of Victoria, P.O. Box 3045 STN CSC, Victoria, BC V8W 3P4, Canada.
E-mail: khouider math.uvic.ca

DOI: 10.1175/JAS3833.1

scales of order 1000 to 3000 km in the lower troposphere as well as the planetary-scale Madden–Julian oscillation (MJO; Dunkerton and Crum 1995; Kiladis et al. 2005; Zhang 2005). Moreover, even if the trimodality is not always evident in nature as seen recently in studies of satellite data for the MJO where the cloud tops follow rather a continuous spectrum, although this is not our primary intention, the three cloud-type approach could be viewed as a crude approximation for this continuous spectrum, in the context of a two vertical mode model.

At the present time, despite much progress in the parameterization of tropical convection, the current generation of general circulation models (GCMs) still fails to reproduce significant features of the observational record for organized tropical convection on both the synoptic and planetary scales (Slingo et al. 1996; Sperber et al. 1997; Moncrieff and Klinker 1997). The reasons for this failure to represent interactions in the Tropics over a wide range of scales is a practical problem of central importance.

One way to address the multiscale organization of convection in the Tropics is through cloud-resolving modeling (CRM) where the fluid equations with bulk cloud microphysics are discretized on small-scale meshes of order a few kilometers while the physical domain is restricted in size to the order of a few thousand kilometers in two or three space dimensions (Grabowski et al. 2000; Tompkins 2001a,b); alternatively, cloud-resolving convective parameterization (CRCP) also called "superparameterization" (Grabowski 2001, 2003) where two different grid meshes are used. The large-scale fluid dynamic and thermodynamic variables are solved on a 3D planetary-scale grid of order [O(12 000) km] and the convective-scale variability, within each large-scale grid box of order O(200) km, is represented by a CRM on a 2D (x–z or y–z) grid. However this induces a scale gap between the CRM scales and the planetary-scale grid that bypasses the synoptic-scale variability. A notable example displaying some features of organized convective superclusters occurs with a CRM model in two dimensions on a 20 000 km domain (Grabowski and Moncrieff 2001) while "MJO-like" patterns occur in recent CRCP studies (Grabowski 2001, 2003).

Another way to develop insight into the parameterization problem for both the climatology and organized large-scale convectively coupled wave fluctuations in the Tropics is through intermediate models parameterizing various aspects of tropical convection with crude vertical resolution (Yano and Emanuel 1991; Yano et al. 1995; Neelin and Yu 1994; Neelin and Zeng 2000; Mapes 2000; Majda and Khouider 2002; Majda et al. 2004). This is the approach utilized in the present paper. Recently the authors have developed a systematic intermediate model convective parameterization highlighting the dynamic role of the three cloud types discussed above with two baroclinic modes of vertical structure (Khouider and Majda 2006a, hereafter KM06a): a deep convective heating mode and a second mode with lower troposphere heating and cooling corresponding respectively to congestus and stratiform clouds. The model includes both a systematic moisture equation where the lower troposphere moisture increases through detrainment of shallow cumulus clouds, evaporation of stratiform rain, and moisture convergence and decreases through deep convective precipitation and also a nonlinear switch, which favors either deep or congestus convection depending on whether the troposphere is moist or dry. All of these effects conspire to produce a new type of convectively coupled instability at large scales with the physical structure of the resulting linearly unstable waves in qualitative agreement with observations (KM06a); in particular, these new multicloud model parameterizations do not rely at all on wind-induced surface heat exchange (WISHE) to create instability (Emanuel 1987; Emanuel et al. 1994). While there is no doubt that WISHE plays an important role in hurricane development (Zehnder 2001; Craig and Gray 1996), there is no observational evidence directly linking the structure of convectively coupled Kelvin waves and two-day waves to WISHE.

The field of intermediate models for tropical convection has evolved enough so that a whole review paper is necessary to summarize all the different approaches and to clarify all the standard parameters. Therefore, due to page limitations, the emphasis here is rather on the novelties introduced in the multicloud models. For further information the reader is referred to the literature (Yano and Emanuel 1991; Yano et al. 1995; Neelin and Zeng 2000; Mapes 2000; Majda and Shefter 2001).

A systematic linear stability analysis around radiative–convective equilibrium (RCE) solutions for the multicloud model convective parameterizations and RCEs is presented in KM06a, in various parameter regimes and for both a weak uniform radiative cooling of $Q_{R,1}^0 = 0.04$ K day^{-1} and the more realistic value of $Q_{R,1}^0 = 1$ K day^{-1}. A detailed nonlinear wave analysis with the weak radiative cooling ($Q_{R,1}^0 = 0.04$) is presented in Khouider and Majda (2006b). In the present paper, the multicloud model convective parameterizations are applied to a 40 000-km periodic equatorial ring without rotation, with a background sea surface temperature (SST) gradient and realistic radiative cooling mimicking a tropical warm pool (Grabowski et al. 2000) with a grid spacing $\Delta x = 40$ km. The goals are to

understand the emerging time mean 2D circulation (climatology) and the convectively coupled wave fluctuations about this climatology including their large-scale organization as well as the dependence of these phenomena on crucial physical parameters in the multicloud model. The multicloud model parameterization and the general numerical setup and diagnostics are described briefly in section 2. The climatology, wave fluctuations, and large-scale wave organization are discussed in a prototype case study in section 3 while section 4 studies the dependence of these results on crucial physical parameters in the parameterization. This is followed by a concluding discussion in section 5.

2. The basic setup

A detailed discussion and presentation of the multicloud convective parameterization utilized here are found in KM06a. However, the governing equations and the key closure equations are outlined briefly below for the sake of completeness. This is then followed by the basic setup utilized here for nonlinear simulations with the multicloud parameterization on a periodic equatorial ring without rotation, with a background SST gradient mimicking the western Pacific/Indian Ocean warm pool.

a. The multicloud parameterization

In the case without rotation and without a barotropic wind, the dynamical core of the multicloud parameterization, introduced and analyzed in KM06a, reads

$$
\begin{aligned}
&\frac{\partial \theta_{eb}}{\partial t} = \frac{1}{\tau_e}(\theta_{eb}^* - \theta_{em}) - \frac{1}{h_b} D\\
&\frac{\partial q}{\partial t} + \frac{\partial}{\partial x}[(u_1 + \tilde{\delta} u_2) q] + \tilde{Q}\left(\frac{\partial u_1}{\partial x} + \tilde{\lambda}\frac{\partial u_2}{\partial x}\right)\\
&\qquad = -\frac{1}{\tau_{\text{conv}}} P + \frac{1}{H_T} D\\
&\frac{\partial H_c}{\partial t} = \frac{1}{\tau_c}\left(\alpha_c \frac{\Lambda - \Lambda^*}{1 - \Lambda^*}\frac{D}{H_T} - H_c\right)\\
&\frac{\partial H_s}{\partial t} = \frac{1}{\tau_s}\left(\frac{\alpha_s}{\tau_{\text{conv}}} P - H_s\right)\\
&\frac{\partial u_j}{\partial t} - \frac{\partial \theta_j}{\partial x} = -C_d(u_0) u_j - \frac{1}{\tau_R} u_j, \quad j = 1, 2\\
&\frac{\partial \theta_1}{\partial t} - \frac{\partial u_1}{\partial x} = \frac{\pi}{2\sqrt{2}}\left(\frac{1}{\tau_{\text{conv}}} P - Q_{R,1}^0\right) - \frac{1}{\tau_D}\theta_1\\
&\frac{\partial \theta_2}{\partial t} - \frac{1}{4}\frac{\partial u_2}{\partial x} = \frac{\pi}{2\sqrt{2}}(-H_s + H_c - Q_{R,2}^0) - \frac{1}{\tau_D}\theta_2,
\end{aligned}
\tag{2.1}
$$

where θ_{eb} is the boundary layer equivalent temperature, q is the vertical average water vapor deviation from an imposed background moisture stratification. Notice that the q equation is normalized by the latent heating constant so that q assumes units of temperature. Here H_c is the congestus heating and H_s is the stratiform heating while θ_j and u_j, $j = 1, 2$ are, respectively, the potential temperature and zonal velocity components associated with the first and second baroclinic–vertical modes. The total zonal velocity and anomalous potential temperature are respectively given by $U(x, z, t) \approx \sqrt{2}\cos(z)u_1(x, t) + \sqrt{2}\cos(2z)u_2(x, t)$ and $\Theta(x, z, t) \approx \sqrt{2}\sin(z)\theta_1(x, t) + 2\sqrt{2}\sin(2z)\theta_2(x, t)$, $0 \le z \le \pi$. Accordingly, the (total) convective heating field is given by $Q_c = (\pi/2)(1/\tau_{\text{conv}})P(x, t)\sin(z) + \pi[H_c(x, t) - H_s(x, t)]\sin(2z)$ by adding the contribution from both θ_1 and θ_2. Here $h_b = 500$ m and $H_T = 16\,000$ km are respectively the heights of the surface boundary layer and the depth of the tropical troposphere. The term P models simultaneously the bulk precipitation and the deep convective heating while D represents the downdrafts, due to detrainment of shallow/congestus clouds and evaporation of stratiform rain, cooling and drying the boundary layer and moistening the middle troposphere at the same time. Notice a slight change in notation compared to KM06a regarding the effective deep convective heating; here the convective time scale τ_{conv} is highlighted directly in (2.1). The quantities $Q_{R,j}^0$, $j = 1, 2$ are imposed uniform radiative cooling rates associated with the first and second baroclinic modes.

In the absence of downdrafts, θ_{eb} relaxes toward a fixed saturation equivalent potential temperature, θ_{eb}^*; which is a function of the sea surface temperature, according to an evaporative time scale, τ_e, of about 8 h consistent with a Jordan-sounding-based homogeneous RCE, see section 2b below. Moreover, $\tau_{\text{conv}} = 2$ h is the deep convective time scale and $\tau_s = \tau_c = 3$ h are respectively the stratiform and congestus adjustment times with $\alpha_s = 0.25$ and $\alpha_c = 0.5$ the stratiform and congestus adjustment coefficients. For other basic coefficients in the model, $\tau_R = 75$ days is the Rayleigh friction time scale and $\tau_D = 50$ days is the Newtonian cooling time scale while $c_d = 0.001$ and $u_0 = 2$ m s^{-1} are the turbulent drag coefficient and turbulent velocity scale. Notice that recent interpretations of observations (Bretherton et al. 2004) suggested longer adjustment times as large as $\tau_{\text{conv}} = 12$ h. Higher values for τ_{conv} are considered, at least for linear stability and nonlinear simulations with the homogeneous state (in Khouider and Majda 2006b).

To achieve proper closures for the precipitation/deep convective heating, P, and the downdrafts, D, a nonlinear switch, Λ, measuring the relative moistness and dry-

ness of the middle troposphere is introduced (Zehnder 2001; KM06a) as a continuous piecewise linear function of the discrepancy between the boundary layer and middle-troposphere equivalent potential temperatures, $\theta_{eb} - \theta_{em}$. The approximate value $\theta_{em} = q + (2\sqrt{2}/\pi)(\theta_1 + \alpha_2\theta_2)$ is used with $\alpha_2 = 0.1$ adds a contribution to θ_{em} from slightly below the middle troposphere. When the discrepancy $\theta_{eb} - \theta_{em}$ exceeds 20 K, the troposphere is cold and dry and Λ is set to one and when $\theta_{eb} - \theta_{em} \leq 10$ K the troposphere is warm and moist we let $\Lambda = \Lambda^* = 0.2$. Therefore the precipitation and downdrafts are closed by

$$P = \frac{1 - \Lambda}{1 - \Lambda^*} P_0^+ \quad \text{and} \quad D = \Lambda D_0$$

with

$$P_0 = [a_1\theta_{eb} + a_2(q - \hat{q}) - a_0(\theta_1 + \gamma_2\theta_2)],$$

$$D_0 = m_0\left(1 + \mu\frac{H_s - H_c}{Q_{R,1}^0}\right)^+(\theta_{eb} - \theta_{em}), \qquad (2.2)$$

where $X^+ = \max(X, 0)$. Here P_0^+ and D_0 are the maximum allowable deep convection (also called precipitation below) and downdrafts, respectively; P_0 can be thought of as a measure of convectively available potential energy (CAPE) and tropospheric water vapor condensation rate where $\hat{q}$ is a threshold beyond which condensation takes place and whose value is specified through the RCE solution (Khouider and Majda 2006a,b). Notice that the present models are not bound to the CAPE or the adjustment-type closures for P_0. Any other parameterization which is thought to be suitable for tropical deep convection could be adopted.

From the expressions for P and D and Eq. (2.1), when the (lower) middle troposphere is dry ($\Lambda = 1$) deep convection is inhibited ($P = 0$) even if P_0 is positive and downdrafts, D, and congestus heating, H_c, are maximized. Whereas when the troposphere is extremely moist ($\Lambda = \Lambda^*$), deep convection is maximized and congestus heating is zero. Notice also that the deep convective scheme described here obeys an adjustment equation with a convective time scale $\tau_{\text{conv}} = 2$ h. Therefore, it belongs to the family of quasi-equilibrium parameterizations such as CAPE and Betts–Miller parameterizations.

b. *Key parameters and basic convective instability mechanisms in the model parameterization*

More details on the definitions and significance of the different coefficients involved in the expressions of P_0 and D_0 above including tables of representative values as well as the dynamical features of the multicloud parameterization are found in KM06a. Nevertheless, the specific parameter values used herein are given below in sections 3 and 4. Especially, the coefficient a_0, which sets a buoyancy time scale for convection (Fuchs and Raymond 2002), and γ_2, which alters the dry static stability of the lower troposphere, play a crucial role in setting both the mean climatology and the strength and organization behavior of the convectively coupled wave fluctuations.[1] In earlier work the authors established that a_0 and γ_2 are the two important parameters for the linear instability of large-scale convectively coupled waves (KM06a) and for the intermittency of convective events in nonlinear simulations with weak convective cooling (Khouider and Majda 2006b). Below, the coefficients a_1 and a_2 fixing the contributions to the deep convective heating from respectively the boundary layer θ_{eb} (i.e., CAPE) and the moisture q are also varied under the constraint $a_1 + a_2 = 1$ to study sensitivity of parameterizations to these variables. The coefficients m_0 and μ_2 involved in D_0 are kept constant herein with the value of m_0 set by the RCE solution (which is dictated by the Jordan sounding; KM06a) and $\mu_2 = 0.5$ (Majda and Shefter 2001; Majda et al. 2004).

In addition to the introduction of the switch function, Λ, assessing and systematically taking into account the moistness and dryness of the middle troposphere, the originality of the present parameterization resides in the systematic derivation of the vertical average moisture equation (KM06a). The moisture content is increased (locally) by both the lower tropospheric moisture convergence from both the first and second (lower troposphere) baroclinic convergences and the moistening from detrainment of shallow/congestus clouds and evaporation of stratiform rain (D effect in q equation) and it decreases from deep convection/precipitation, P. The constants $\tilde{\delta} = .1$, $\tilde{Q} = .9$, and $\tilde{\lambda} = .8$ fix the strength of the linear and nonlinear moisture convergence from the first and second baroclinic modes. The physical justification for these values is found in KM06a and the references therein. In turn, P increases with θ_{eb} and q and it decreases with increasing (lower) middle tropospheric dry static stability, $\theta_1 + \gamma_2\theta_2$. The boundary layer θ_{eb} increases through evaporation from the sea surface and decreases by downdraft cooling and drying. In turn the downdrafts increase with increasing stratiform rain and decrease with increasing congestus heating. This last feature reflects the fact that congestus

[1] Notice that although there is a mathematical relationship between a_0 and the buoyancy relaxation time scale of Fuchs and Raymond, here it has a radically different physical effect on the present model mainly because of the second baroclinic potential temperature in the term $\theta_1 + \alpha_2\theta_2$.

heating warms the lower troposphere thus it reduces the detrainment of congestus clouds.

Furthermore, the surface fluxes are reduced to a simple relaxation scheme for the boundary layer θ_{eb} without any WISHE effect (Emanuel 1987; Emanuel et al. 1994) and yet the multicloud parameterization displays instability, in realistic parameter regimes, at large scales of convectively coupled gravity waves with physical features qualitatively resembling those of observed tropical Kelvin waves (Wheeler and Kiladis 1999), as demonstrated in KM06a. Also this instability is not a convective instability of the second kind (CISK; Charney and Eliassen 1964; Lindzen 1974, etc.) because, in the present model, the low-level moisture convergence is not directly converted into convective heating as in traditional CISK models but it is used to raise locally the moisture level, which in turn increases P_0; that is, the potential for deep convection, which rather obeys an adjustment scheme. Deep convection is triggered only if the troposphere is sufficiently moist, through the switch function Λ in addition to the boundary layer and the stratiform and congestus heating features. The combined effect has the (desired) consequence that, unlike the traditional CISK models, in the realistic parameter regimes, the model is stable at small and mesoscopic scales. Also the main physical mechanisms responsible for this new instability are different from those behind stratiform instability (Majda and Shefter 2001; Majda et al. 2004). Linear theory revealed that it is because of the combined effects of the low-level dry static stability (parameter γ_2) and the second baroclinic moisture convergence (parameter $\tilde{\lambda}$; KM06a). By cooling and converging moisture into a localized region one creates the necessary conditions for condensation to occur and thus promoting convection in an atmosphere whose lower-tropospheric dry stability is already reduced. Moreover, when the boundary layer equivalent potential temperature is switched off in the multicloud model (results not shown), the range of unstable mode does not expand toward small scales and the wave CISK catastrophe does not occur but the instability of the moist gravity waves become very weak and confined to small wavenumbers.

c. The basic framework with an SST gradient

We consider a realistic homogeneous radiative cooling of $Q^0_{R,1} = 1$ K day^{-1}. Notice that, according to (2.1) the effective radiative cooling has a maximum in the middle troposphere of $\pi/(2\sqrt{2})\ Q^0_{R,1}$, which is actually slightly larger than 1 K day^{-1}. According to recent observations, cooling rates in the tropical atmosphere could be as large as 2 K day^{-1}. When the discrepancy between the boundary layer saturation equivalent potential temperature (which is a function of SST) and the boundary layer equivalent potential temperature at RCE is fixed to $\theta^*_{eb} - \overline{\theta}_{eb} = 10$ K, consistently with the tropical Jordan sounding (e.g., Gill 1982), the boundary layer evaporative heating at RCE is given by $(1/\tau_e)$ $(\theta^*_{eb} - \overline{\theta}_{eb}) = (H_T/h_b)Q^0_{R,1} = 31.5$ K day^{-1} according to a fixed evaporative time scale of $\tau_2 \approx 8$ h.

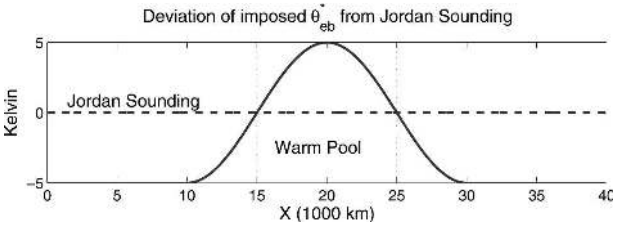

FIG. 1. SST gradient profile mimicking a warm pool region.

In this study we consider a nonuniform sea surface temperature with a zonal gradient mimicking the Indonesian warm pool. Over the 40 000-km domain, θ^*_{eb} is raised from its Jordan sounding value to up to 5 K in the center of a 10 000-km warm pool region, centered in the computational domain, and is diminished by up to 5 K outside this warm pool region (Grabowski et al. 2000; Bretherton and Sobel 2002). These associated maximum and minimum values are joined by a (full) sine function within a 20 000-km region and constant elsewhere, as depicted in Fig. 1.

To discretize the system of equations in (2.1) we adopt a fractional step operator splitting strategy where the x-derivative conservative terms on the left-hand side are handled by a high-order nonoscillatory central scheme and the right-hand side remaining ODEs are integrated by a second-order Runge–Kutta method. The interested reader is referred to Khouider and Majda (2005a,b).

Starting with a homogeneous RCE solution corresponding to the Jordan sounding forcing, depicted by a dashed line in Fig. 1, as initial conditions, we integrate the equations in (2.1) for about 800 days. A grid mesh size $\Delta x = 40$ km and a time step $\Delta t = 2$ min [far below the Courant–Friedrichs–Lewy (CFL) constraint of about 15 min] are utilized. After a transient period of about 100 to 200 days, the solution reaches a statistical steady state as illustrated in Fig. 2 where the root mean square (rms) of all the prognostic variables, u_j, θ_j, $j = 1$, 2, θ_{eb}, q, H_s, H_c, are plotted in time along the 800 days integration period, for the typical case (control run) with $a_0 = 10$, $a_1 = 0.1$, $a_2 = 0.9$, $\gamma_2 = 0.1$, $\alpha_c = 0.5$, and the standard forcing depicted in Fig. 1. In sections 3 and 4 below we illustrate and analyze the results of the nonlinear simulations when some of the multicloud model parameters are varied. The list of all the cases

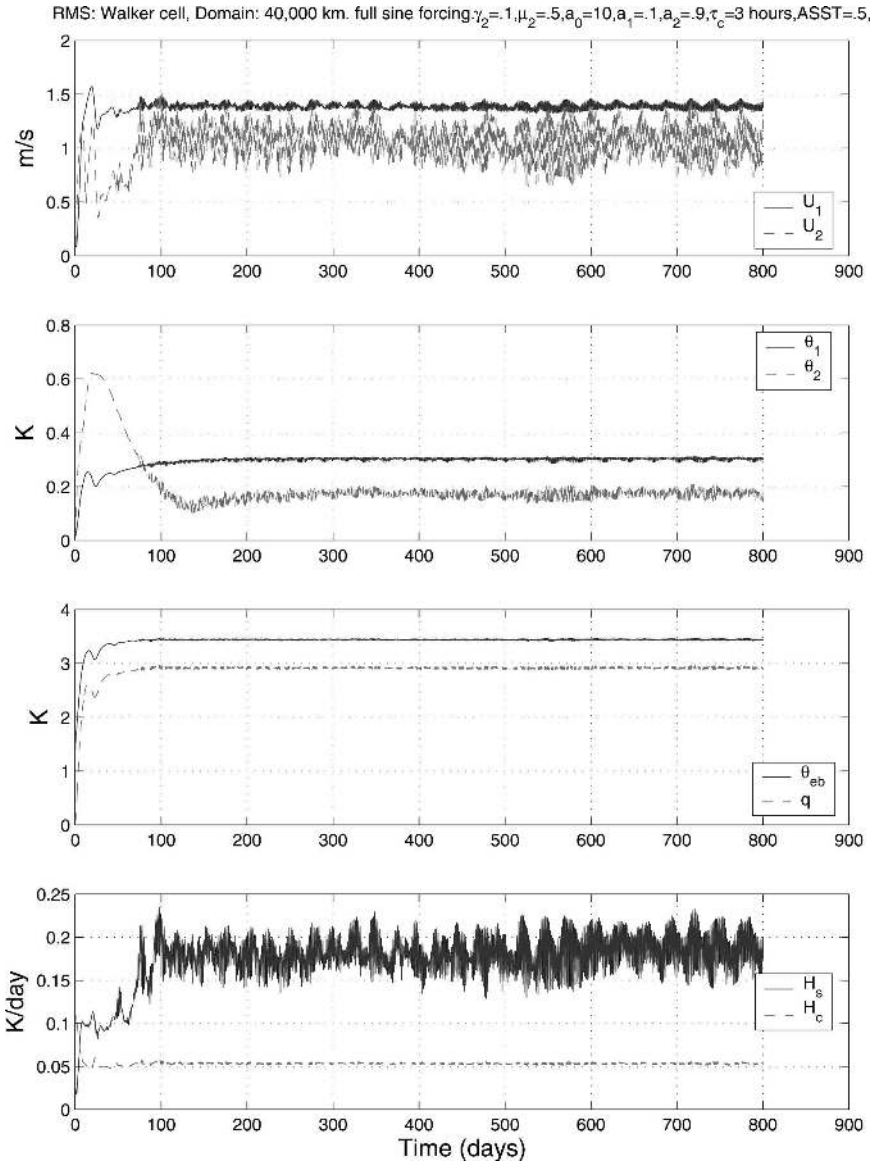

FIG. 2. History of the rms of the deviations from the homogeneous RCE initial conditions for the prognostic variables, u_j, θ_j, θ_{eb}, q, H_s, H_c in the multicloud model using the standard warm pool forcing along the integration time period of 800 days with the parameters $a_0 = 10$, $a_1 = 0.9$, $a_2 = 0.1$, $\gamma_2 = 0.1$, $\alpha_c = 0.5$ (case 1).

considered herein is given in Table 1. For each case, the solution components are averaged in time over the last 500 days of simulation and both the associated climatology and the wave fluctuations about it are compared to the control run where a classical Walker-type circulation is obtained, as illustrated in Figs. 3 and 4 below. We begin by contrasting and summarizing these results in Table 2 where, in the second column, it is stated whether the time-averaged flow is a Walker-type circulation while the maximum of the mean flow and the maximum standard deviation of the wave fluctuations are given in terms of the first and second baroclinic velocity components, u_1 and u_2, in columns 3, 4 and 5, 6, respectively. The details of these results and their analysis are reported in sections 3 and 4 below.

3. Prototype simulations

Here we present and analyze the results obtained for the prototype simulation corresponding to the parameter regime in case 1 of Table 1 with $a_0 = 10$, $a_1 = 0.9$, $a_2 = 0.1$, $\gamma_2 = 0.1$, $\alpha_c = 0.5$ and the standard warm pool

TABLE 1. List of parameter regimes used for warm pool simulations.

	a_0	a_1	a_2	γ_2	α_c	Warm pool forcing
Case 1	10	0.1	0.9	0.1	0.5	Standard
Case 2	10	0.1	0.9	0.1	0.5	Doubled
Case 3	10	0.1	0.9	0.1	2	Standard
Case 4	20	0.1	0.9	0.1	0.5	Standard
Case 5	7.5	0.1	0.9	0.05	0.5	Standard
Case 6	7.5	0.5	0.5	0.1	0.5	Standard
Case 7	7.5	0.75	0.25	0.1	0.5	Standard
Case 8	4	0.1	0.9	0.05	0.5	Standard

forcing of Fig. 1. We begin in Fig. 3a with the zonal-time contour plots (Hovmöller diagram) of the deep convective forcing $(1/\tau_{\text{conv}})P(x, t)$–a surrogate for precipitation on the whole 40 000-km computation domain and during the last 500 days of simulation (discarding the first 300 days transient period). From Fig. 3a, the statistical equilibrium between 300 and 800 days is characterized by highly chaotic and intermittent deep convective events of moderate to relatively strong heating rates varying between 2 to 5 K day^{-1} localized within the warm pool region extending between 15 000 to 25 000 km. Outside this region the precipitation rates are very weak and only some rare convective patches with heating rates between 1.5 and 2 K day^{-1} are visible. Figures 3b,c display the probability density distributions (PDFs) of the deep convective rates during the last 500-day period of simulation outside and inside the warm pool region, respectively. The PDFs in Figs. 3b,c depict a delta-like peak at zero in agreement with the physical intuition that deep convection in the Tropics is characterized by relatively rare and intermittent events dominated by congestus and shallow convection and/or clear sky periods. Nevertheless, both the inside and outside PDFs display a second much weaker but smoother peak at around $(1/\tau_{\text{conv}})P = 1$ K day^{-1} and $(1/\tau_{\text{conv}})P = 1.25$ K day^{-1}, respectively, with a much wider tail for the inside PDF.

a. Climatology

In Figs. 4a,b, we plot the mean velocity and potential temperature components, respectively, the boundary layer θ_{eb} and the vertical average moisture content q on Fig. 4c, and the stratiform and congestus heating rates on Fig. 4d. From Fig. 4, the mean flow exhibit a dominant first baroclinic velocity component with a strong convergence located at the center of the warm pool which is counterbalanced by a much weaker second baroclinic divergence. Away from the center the first baroclinic velocity has a positive slope suggesting a Walker-like mean circulation where (moist and warm) air rises from the surface within the warm pool while elsewhere in the domain (dry and cold) air descends. From Fig. 4b, with spatial variations not exceeding 0.5 K for θ_1 and 0.2 K for θ_2, the mean potential temperature exhibits a weak temperature gradient whereas the boundary layer θ_{eb} and the moisture q in Fig. 4c, respectively, peak by up to 7 and 5 K at the center of the warm pool as a result of the relatively vigorous deep convective activity within this region, leaving the rest of the troposphere, outside the region above the warm pool, relatively cold and dry. The stratiform and congestus heating rates also peak at the center of the warm pool but they both exhibit troughs of low mean heating near the warm pool boundaries; within the regions between 10 000 and 15 000 km and 25 000 and 30 000 km.

The Walker circulation conjectured above is confirmed through the x–z profile of the mean flow (arrows) overlaid on the mean convective heating and mean potential temperature fields in Figs. 5a,b. The time-averaged flow displayed in Figs. 5a,b represents the prototype Walker-type circulation in the multicloud model parameterizations with moist and warm air rising from the surface within the warm pool region and cold and dry air sinking to the ground elsewhere in the domain. Nevertheless, this descending branch is stronger in the regions near the boundaries of the warm pool at the locations between 10 000 and 15 000 km and 25 000 and 30 000 km associated with the heating troughs seen in Fig. 4d. From Fig. 5a, consistent with the precipitation plots in Fig. 3, the region of ascending flow is associated with stronger convective heating in the middle of the troposphere.

b. Large-scale organization and fluctuating waves

Notice from Fig. 3a that the bulk variability is organized into large-scale patterns slowly moving to the left (westward). Since the beta effect is ignored, eastward- and westward-propagating waves can coexist and interact with each other, however, more often due to the randomness in the initial conditions, one direction may take over the other as the waves in that direction amplify first and stabilize the environment around them (Khouider and Majda 2006b). Overall, the velocity fluctuations are relatively weak outside the warm pool region where there is little deep convective heating.

Figure 6a shows the energy spectrum of the deep convective field, $(1/\tau_{\text{conv}})P(x, t)$, over the 500 days period as shown in Fig. 3a. Apparent from Fig. 6a are low-frequency peaks varying on time scales in the range of 10 to 20 days and smaller corresponding to structures moving roughly at 3 m s^{-1}; westward for the most sig-

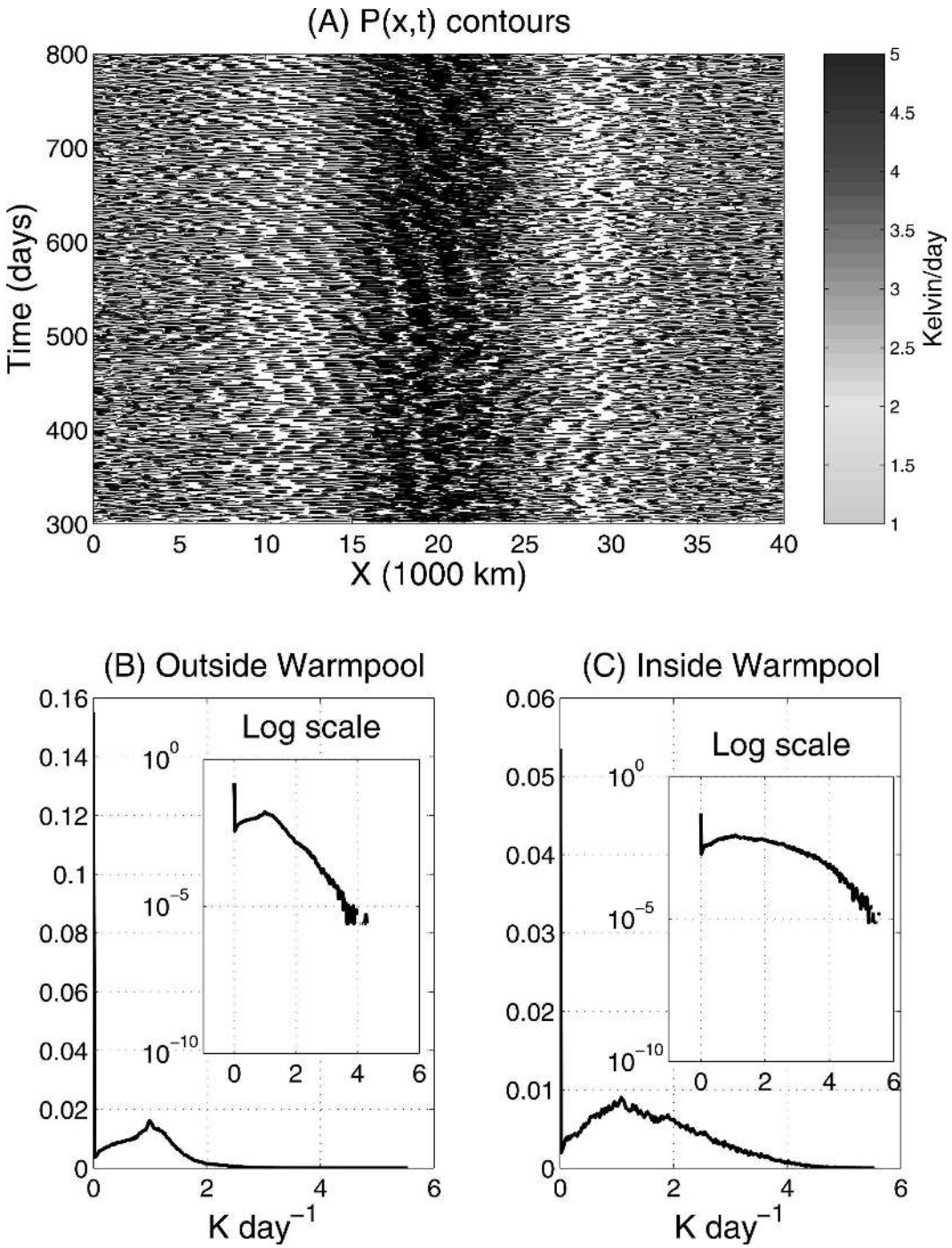

FIG. 3. Deep convective activity. (a) Contour plots of the deep convection, $(1/\tau_{\text{conv}})P(x, t)$, over the 40 000-km domain for the last 500 days. PDFs of deep convection (b) outside and (c) inside the warm pool region. Bins are normalized by the corresponding number of grid points (x_i, t_n) outside and inside the warm pool. Logarithmic scale plots of the PDF's are superimposed (case 1).

nificant peaks on the left half of the domain, with a zonal scale of roughly 2000 km as shown by the arrow. These spectral signals correspond to the large scale slowly moving patterns seen in Figs. 3a. The next frequency band of significant spectral peaks, on Fig. 6a, concerns structures varying on the order of 3 to 4 days and move in both directions at roughly 17 m s^{-1}. These have a spatial scale on the order of 5000 km and less.

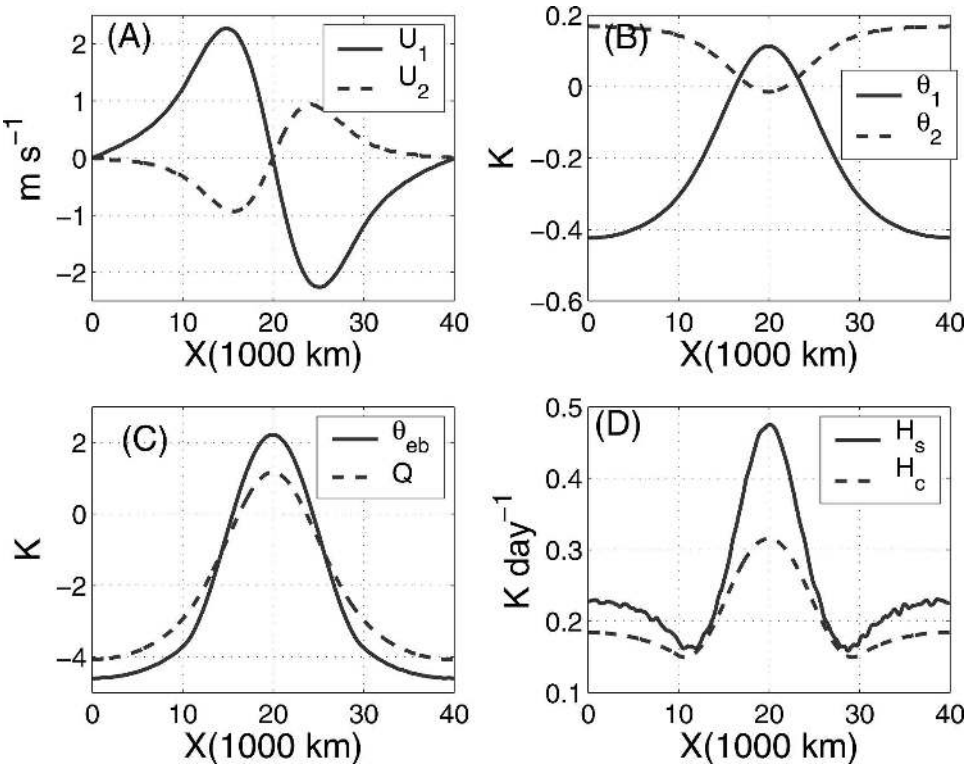

FIG. 4. Zonal structure of the diagnostic variables, u_j, θ_j, θ_{eb}, q, H_s, H_c, averaged over the last 500 days of simulation for the typical case 1 in Figs. 2 and 3.

Notice the peak corresponding to eastward moving features (on the right) is more significant. Higher frequency signals (up to close to 2 days) are also apparent on this figure. Figure 6b shows the color filled contours of the deep convective heating in the left region of the domain between 0 and 25 000 km, including the warm pool region, for the time period from 650 to 700 days. Figures 6a,b clearly show that the patterns seen in Figs. 3a consist indeed of envelopes of large-scale convectively coupled wave packets. These envelopes evolve inside the warm pool and slowly move to the left (westward) and expand and weaken as they leave the warm pool. At least two of these envelopes are distinguishable in Fig. 6b within the warm pool region. One evolves roughly between times 660 and 685 days and the other starts roughly at time 685 days and lasts beyond the time 700 days limiting the contour plot. The straight line connecting the centers of maximum con-

TABLE 2. Comparative chart summarizing the numerical results for the cases in Table 1.

	Walker cell climatology	Maximum mean horizontal wind (m s^{-1})		Maximum standard deviation (m s^{-1})	
		$\overline{U}_1$	$\overline{U}_2$	u_1	u_2
Case 1	Yes	2.2643	0.92	0.7963	1.4342
Case 2	Yes	4.4320	1.7642	1.4542	2.5850
Case 3	No	0.7003	0.6931	5.7940	15.2548
Case 4	Yes	1.6262	0.7224	0	0
Case 5	Yes	2.2521	0.8588	2.08723	4.8941
Case 6	Yes	2.5754	0.9393	2.2191	5.6174
Case 7	Yes	2.2797	0.8424	2.2346	4.7706
Case 8	No	2.4632	0.9292	5.1174	9.2155

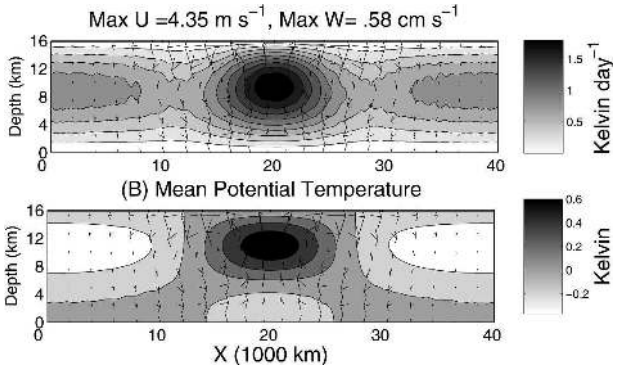

FIG. 5. The x–z structure of the time-averaged flow for case 1 in Fig. 4. (a) Convective heating and (b) potential temperature anomalies with the (u, w) flow profile overlaid.

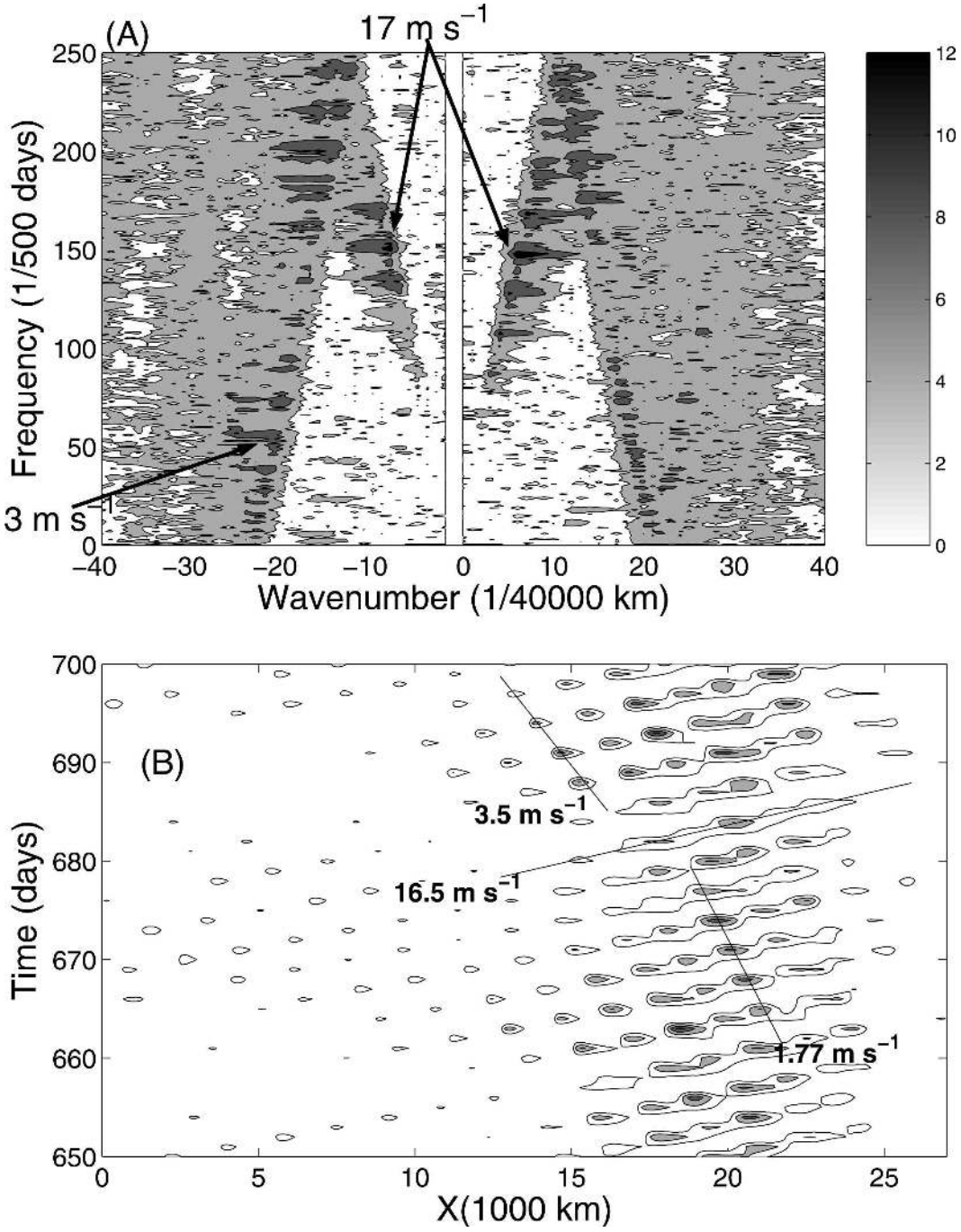

FIG. 6. Case 1: (a) Deep convective energy spectrum. The spectral peaks corresponding to the westward-moving envelopes and eastward- as well as westward-moving waves are highlighted. (b) Regions of deep convective heating exceeding 2, 3, and 4 K day^{-1} on a smaller space–time domain showing wave packets moving to the right at about 16.5 m s^{-1} and two of their convective peak envelopes moving westward at roughly 1.77 and 3.5 m s^{-1}.

vective intensity for the first envelope shows a propagating speed of 1.77 m s^{-1} while the most left edge of the upper envelope seems to move at about 3.5 m s^{-1} as demonstrated by the associated straight line. Embedded within the deep convective envelopes are eastward moving wave packets with a phase speed around 16 m s^{-1} associated with convectively coupled moist gravity waves.

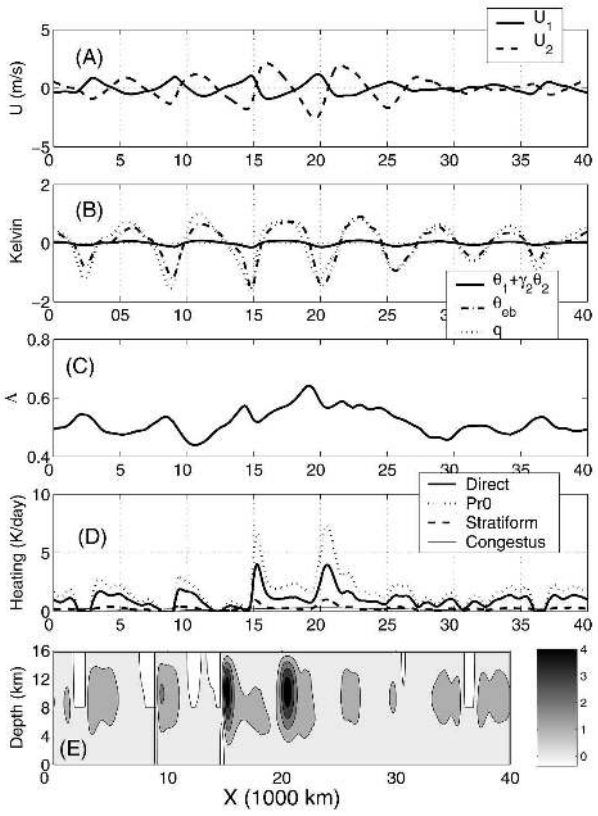

FIG. 7. Deep convective wave traces at day 688. (a) Zonal velocity fluctuations, (b) fluctuations of the dry static stability, $\theta_1 + \gamma_2\theta_2$, the boundary layer θ_{eb}, and the vertical average moisture content, q. (c) The nonlinear switch function, Λ, (d) deep convective, $(1/\tau_{\text{conv}})P$, stratiform, H_s, and congestus, H_c, heating rates with the maximum allowable deep convective heating, $(1/\tau_{\text{conv}})P_0^+$. (e) The x–z structure of the total convective heating field (see text; case 1).

The detailed zonal structure of the wave fluctuations at time 688 days is plotted in Figs. 7a–d, for the zonal velocity components, u_1 and u_2, the thermodynamic quantities, $\theta_1 + \gamma_2\theta_2$ (dry static stability), the boundary layer θ_{eb}, and the moisture q, entering in the convective closure in (2.2), the switch function Λ measuring the dryness of the middle troposphere, and the heating rates, $(1/\tau_{\text{conv}})P$, H_s, H_c, including the maximum allowable deep convective heating, $(1/\tau_{\text{conv}})P_0^+$ (a certain measure of CAPE). Notice that the actual value of H_c in Fig. 7d is amplified by a factor of 10 to highlight its variability with the waves. Moreover, the x–z contours of the total convective heating field, $(1/\tau_{\text{conv}})P(x, t)\sin(z) + 2[H_c(x, t) - H_s(x, t)]\sin(2z)$, are shown in Fig. 7e. Notice that the heating rates in Fig. 7e are in quantitative agreement with observations as well as CRM simulations (Tulich et al. 2007). Apparent from the plots in Fig. 7 are two dominant structures localized within the warm pool on the right of $x = 15\,000$ km and $x = 20\,000$ km respectively. According to the Hovmöller diagram in Fig. 6, those structures represent the traces of two large-scale (individual) convectively coupled waves moving eastward at roughly 16 m s^{-1}, which are embedded within the 1.77 m s^{-1} westward-moving envelope. Also note the strong signatures of those waves on all the variables plotted in Figs. 7a–d, except for the congestus heating, which is only slightly disturbed. Nevertheless, these small variations in congestus heating seem to be very important for the intermittency of convection. The induced lower-troposphere warming behind the deep convective episodes is key for the stabilization of the middle troposphere for deep convection (because the increase in θ_2 induces a decrease in P_0), which in turn induces an accumulation of water vapor (which can be regarded as coming from the evaporation of shallow/congestus clouds).

Notice the low-level convergence from the first baroclinic velocity overcoming the second baroclinic divergence at the centers of the deep convective regions resulting in a net upward motion over the whole troposphere whereas ahead of the deep heating peaks, the second baroclinic convergence dominates; thus providing the low-level moisture convergence necessary to sustain deep convection-moistening and preconditioning. This mechanism happens in concert with the congestus heating, which becomes more significant away from the deep convective regions. Also the net low-level convergence from the second baroclinic mode translates into upward motion within the lower troposphere accounting for shallow/congestus convection. In addition, the dry static stability ($\theta_1 + \gamma_2\theta_2$) decreases ahead of the convective regions and is followed by an increase in θ_{eb} thus provoking a conditional instability by raising P_0 (i.e., CAPE regeneration stage). Next, the moisture level is restored thanks to the congestus moistening and second baroclinic (low level) convergence, which helps decrease the value of the switch function Λ. Notice that all of U_2, q, θ_{eb} rise in front of the deep convective region with θ_{eb} slightly ahead. Recall form Eq. (2.2) that an increase in q and/or in θ_{eb} is necessary for deep convection to occur. The raise of U_2 in front of the wave follows directly from the fact that a negative slope in U_2 within and slightly behind the convective region implies upward motion in the upper troposphere from stratiform heating and a positive slope in U_2 ahead of the wave is associated with lower tropospheric heating from congestus clouds. Also the rising in U_2 ahead of the wave provides the (low level) moisture convergence, which helps raise further q as pointed above. This in turn leads to the amplification of deep convection, which then consumes moisture and

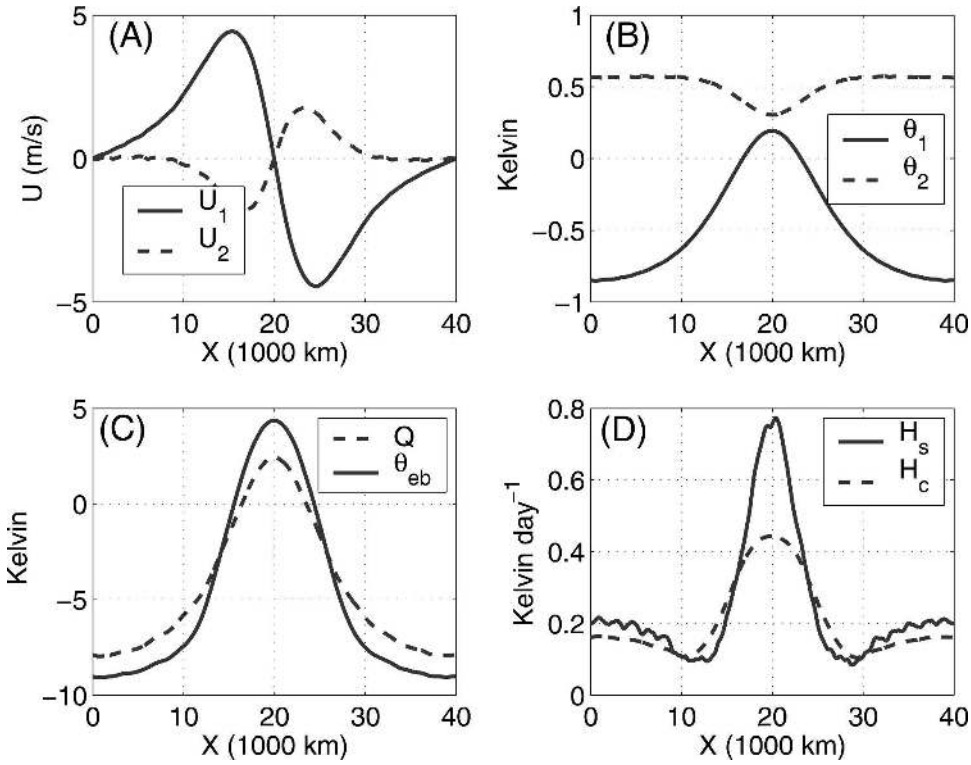

FIG. 8. Same as Fig. 4 except for case 2 with a stronger warm pool forcing.

CAPE. More details about the mechanisms behind the convective instability and the large-scale convective cycle associated with the multicloud parameterizations are found in KM06a and Khouider and Majda (2006b). However, there are some small differences with respect to the nonlinear dynamics between the present runs and the simulations presented in Khouider and Majda (2006b) with weaker radiative cooling. For example, in the present study, the dry static stability drops rapidly after the passage of deep convection, before the θ_{eb} regeneration episode, due to the realistically high radiative cooling utilized here.

From Fig. 6, outside the warm pool region, the convectively coupled waves are relatively weak, and the deep convective peaks are more than 50% smaller than the two dominant peaks located within the warm pool region between 15 000 and 25 000 km. Nevertheless, the congestus heating and the second baroclinic velocity component remain fairly strong outside the warm pool region, making the convectively coupled waves outside the warm pool more or less second baroclinic dominated–congestus waves. The same discrepancy can be seen readily in the convective heating profile in Fig. 7d where the weaker convective region located for example near 10 000 km has more significant congestus heating (visible from the cooling anomalies in the upper troposphere)[2] ahead of the deep convective unlike the deep convective region located within the warm pool.

c. Stronger SST forcing

Here, we double the warm pool SST forcing by raising the boundary layer saturation equivalent potential temperature, θ^*_{eb}, by up to 10 K inside the warm pool region and lower it by −10 K at the extremities of the domain with respect to the Jordan sounding instead of the +5 K and −5 K depicted in Fig. 1 and used in the previous simulation. After a transient period of about 150 days, the solution approaches a statistical steady state where the time averaged mean flow is again a Walker-type circulation. As seen in Table 2, the strength of both the time-averaged flow and the wave fluctuations are accordingly nearly doubled. However, from the zonal plots of the time-averaged solution (over the last 500 days) in Fig. 8, except perhaps for the velocity and potential temperature components in Figs. 8a,b, the rest of the plots show some major differences; especially, from Fig. 8d, the mean congestus heating overshoots the mean stratiform heating at the heating

[2] Recall that in the multicloud model congestus clouds are opposed to stratiform clouds in the sense that they heat the lower troposphere and cool the upper troposphere.

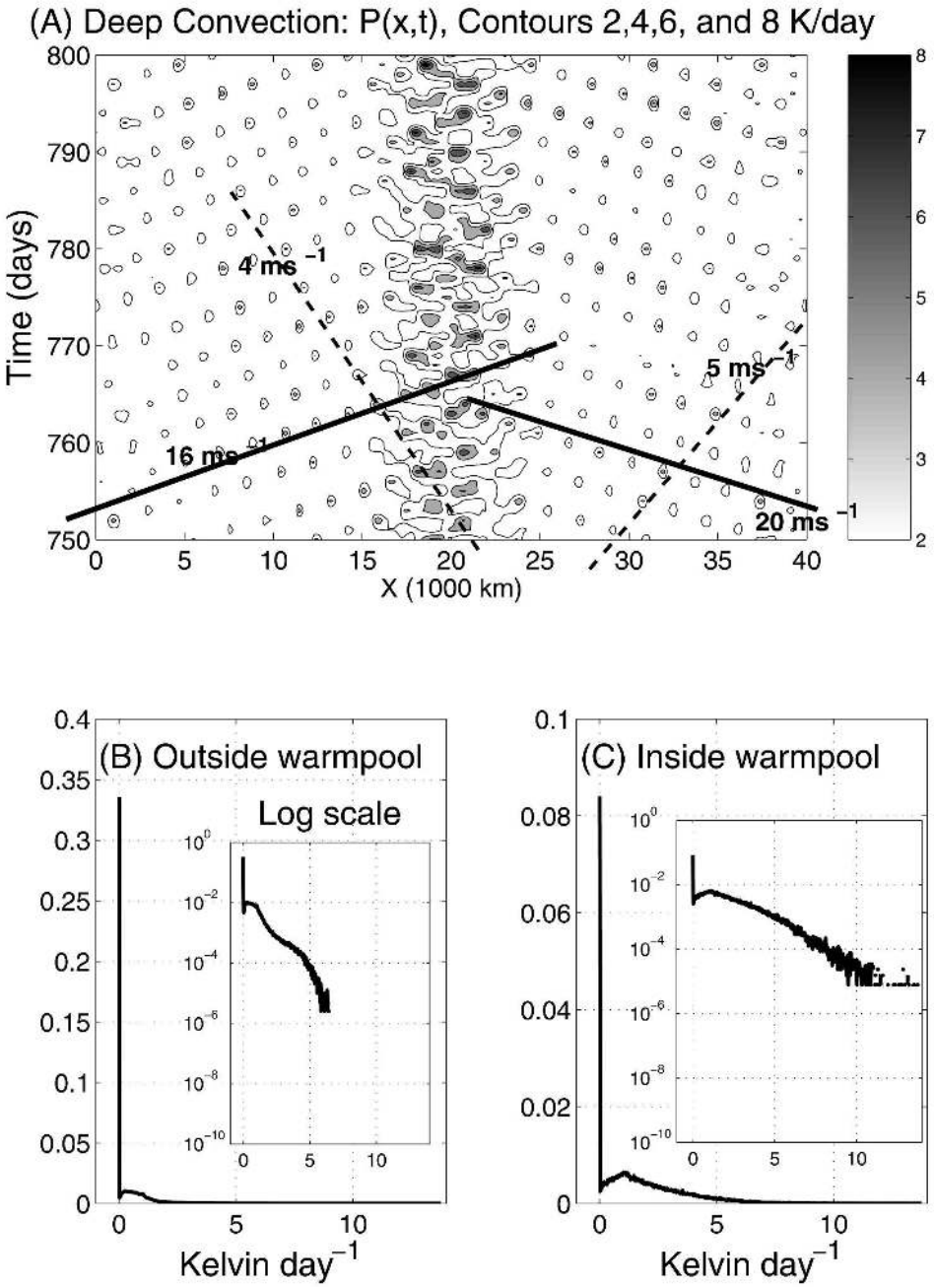

FIG. 9. Deep convective activity for case 2 with a stronger warm pool forcing. (a) Shaded contours for the period 750 to 800 days and for the whole computation domain. (b), (c) PDFs of the convective activity outside and inside the warm pool, respectively. Dashed lines highlight wave tracks moving toward the center and their convective peaks moving away from the warm pool with a slower group velocity.

troughs near the boundaries of the warm pool. Also the q and θ_{eb} profiles in Fig. 8c cross each other a little further from the warm pool boundaries making the moisture profile relatively steeper; that is, the troposphere outside the warm pool is much drier than in the previous simulation with the standard SST forcing.

Other major differences between the present and the previous run are seen in the x–t contour plots of the deep convective heating, $(1/\tau_{\text{conv}})P(x, t)$, for the 50-day period starting at time 750 days, shown in Fig. 9a. The large-scale wave packet envelopes seem to overlap on each other and they become hardly distinguishable.

Nevertheless, while the individual waves are moving toward the warm pool from both sides of the domain with a phase velocity of about 16 to 20 m s^{-1}, the convective peaks of comparable intensity more or less fall on straight lines with a slope directed outward from the center and varying from 4 to 5 m s^{-1}. The large-scale convectively coupled waves moving toward the center of the warm pool from both sides of domain meet within the warm pool region and form large bursts of deep convection.

Moreover, the strength of the deep convection seem to be roughly doubled in both the inside and the outside of the warm pool and the deep convective events exceeding 2 K day^{-1} seem to be less intermittent and more regular outside the warm pool when compared to the control run but events exceeding 4 K day^{-1} are still very rare and chaotic. The PDFs in Figs. 9b,c of the convective activity respectively outside and inside the warm pool are both skewed toward higher heating values. However, while the outside PDF in Fig. 9b shows zero probability for convective events exceeding 6 K day^{-1}, the inside PDF in Fig. 9c displays bursts of very rare events of up to 10 to 14 K day^{-1} as highlighted by the associated blowup plots. Also the convective events outside the warm pool peak at some value below 1 K day^{-1} while inside the warm pool the PDF peaks at a value slightly larger than 1 K day^{-1}. The fact that the two PDFs peak at around 1 K day^{-1} is no surprise given the imposed uniform radiative cooling of 1 K day^{-1}. Therefore, by increasing the SST gradient, the most probable deep convective events remain the same but stronger convective events become probable both inside and outside the warm pool with a highly skewed PDF with a broad tail for more intense events within the warm pool.

d. Role of convective buoyancy frequency

As depicted in Table 2, when the coefficient of the dry static stability, a_0, also called here convective buoyancy frequency (Fuchs and Raymond 2002) is increased to $a_0 = 20$, the Walker circulation is preserved but the convective fluctuations vanish. This in essence confirms the linear stability analysis results in KM06a and the physical intuition that the increase of the convective buoyancy frequency, a_0, enhances the effect of the dry static stability and thus reduces the conditional instability; very small perturbations in $\theta_1 + \gamma_2\theta_2$ can flip the sign of P_0 and make it negative inhibiting further buildup of CAPE. As demonstrated in Khouider and Majda (2006b) for the case with a weaker radiative cooling, increasing a_0 leads to more regular and less intermittent precipitation patterns but with weaker and weaker amplitudes. Ultimately, those amplitudes vanish and the system becomes stable as it is the case here because the higher radiative cooling utilized here decreases further the time interval between successive deep convective events following a given convectively coupled wave track.

In general, increasing the coefficient a_0 makes the established Walker circulation RCE (slightly) weaker and stable while decreasing a_0 amplifies the mean flow and the wave fluctuations and ultimately alters the structure of the Walker circulation as illustrated in section 4 below for the case with $a_0 = 4$.

4. Sensitivity to convective parameters

Here we report the results of four simulations with different values of the convective parameters a_1, a_2, and γ_2 in (2.2). More precisely, we consider the three cases 5, 6, and 7 reported, respectively, in Tables 1 and 2 with fixed $a_0 = 7.5$ and $a_1 = 0.1$, $a_2 = 0.9$, $\gamma_2 = 0.05$; $a_1 = 0.5$, $a_2 = 0.5$, $\gamma_2 = 0.1$; $a_1 = 0.75$, $a_2 = 0.25$, $\gamma_2 = 0.1$. These three cases have different proportions of CAPE, moisture, and dry entropy contributions to the deep convective parameterization in (2.2) but share the common feature that linearized instabilities at the mean Jordan sounding occur only at large scales with a growth rate of roughly 0.5 K day^{-1}. Also case 8 with lower $a_0 = 4$ and $a_1 = 0.1$, $a_2 = 0.9$, $\gamma_2 = 0.05$ is briefly discussed as an extreme example.

a. Climatology

As summarized in Table 2, all the three cases with $a_0 = 7.5$ exhibit a climatology of Walker-type similar to the ones depicted in Figs. 4, 5 and Fig. 8 for cases 1 and 2, respectively. The strength of the mean flow and of the wave fluctuation is essentially the same for these three cases. Nevertheless, some tendency of having stronger first baroclinic wave fluctuations, weaker second baroclinic wave fluctuations, and overall weaker mean flow when passing from case 6 with $a_1 = 0.5$, $a_2 = 0.5$ to case 7 with $a_1 = 0.75$, $a_2 = 0.25$ is noticeable as the deep convective scheme for P_0 shifts toward a θ_{eb} (i.e., CAPE) dominated parameterization with respect to the moisture contribution $a_2(q - \hat{q})$. The mean velocity components and the mean moist thermodynamic variables, θ_{eb} and q, for these three cases are plotted in Figs. 10a,c,e and Figs. 10b,d,f, respectively. Clearly both the velocity and thermodynamic profiles exhibit a lot of similarities when compared to their counterparts in Figs. 4 and 8, including the variations in the positive slopes of U_1, controlling the strength of the descending

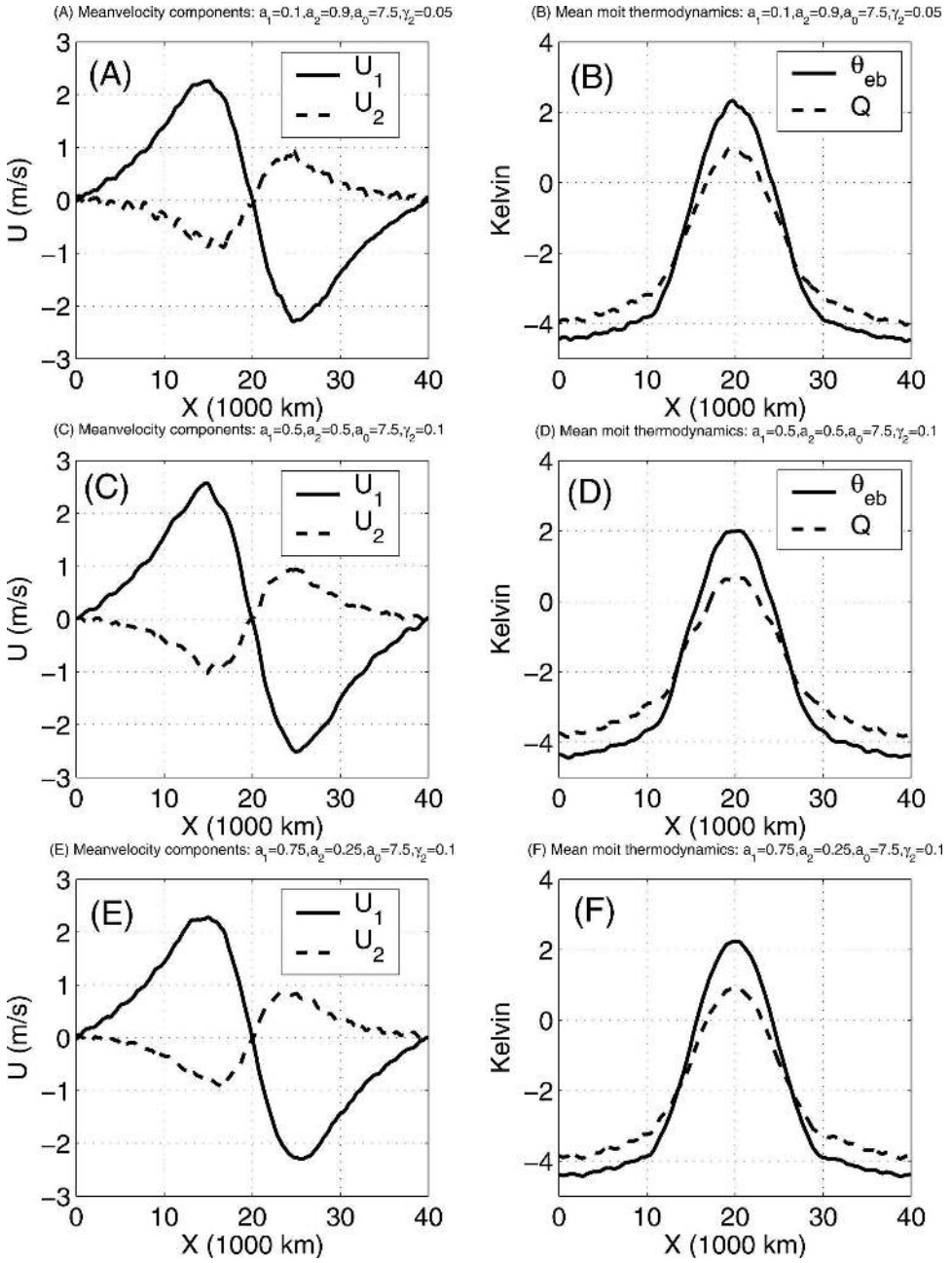

FIG. 10. Sensitivity to convective parameters. Structure of time-averaged (a), (c), (e) velocity components and (b), (d), (f) moist thermodynamics; (a), (b) case 5 with $a_1 = 0.1$, $a_2 = 0.9$, $a_0 = 7.5$, $\gamma_2 = 0.05$, $\alpha_c = 0.5$; (c), (d) case 6 with $a_1 = 0.5$, $a_2 = 0.5$, $a_0 = 7.5$, $\gamma_2 = 0.1$, $\alpha_c = 0.5$; (e), (f) case 7 with $a_1 = 0.75$, $a_2 = 0.25$, $a_0 = 7.5$, $\gamma_2 = 0.1$, $\alpha_c = 0.5$.

branch of the Walker cell, near and away from the warm pool region.

b. Large-scale organization and fluctuating waves

The x–t contours of the deep convection, $(1/\tau_{\text{conv}})P(x, t)$, are shown in Figs. 11(a1),(b1),(c1) for the cases 5, 6, and 7, respectively, while the corresponding PDFs of convective activity outside and inside the warm pool region are plotted in Figs. 11(a2),(a3),(b2),(b3),(c2),(c3), respectively. Clearly, the convective events are still more intermittent outside than inside the warm pool region. The wave fluctuations have considerably increased when compared to the reference case 1 with $a_0 = 10$ for all three convective parameterizations al-

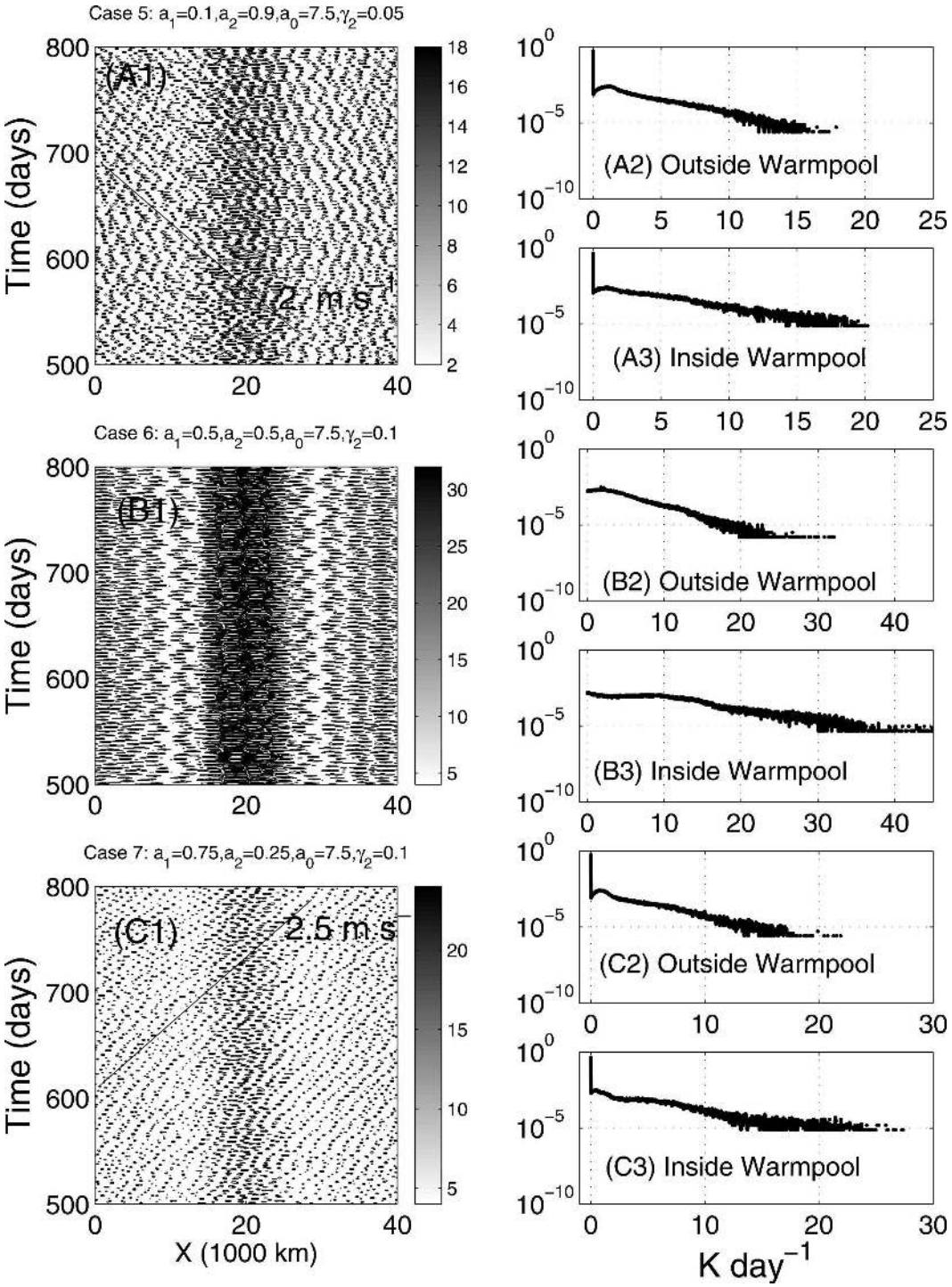

FIG. 11. Sensitivity to convective parameters: (a2), (b1), (c1) Hovmöller diagram of deep convective heating and (a1), (a3), (b2), (b3), (c2), (c3) statistics of deep convective activity outside and inside the warm pool. Scale bar labels are in K day^{-1}. (a) Case 5 with $a_1 = 0.1$, $a_2 = 0.9$, $a_0 = 7.5$, $\gamma_2 = 0.05$, (b) case 6 with $a_1 = 0.5$, $a_2 = 0.5$, $a_0 = 7.5$, $\gamma_2 = 0.1$, and (c) case 7 with $a_1 = 0.75$, $a_2 = 0.25$, $a_0 = 7.5$, $\gamma_2 = 0.1$.

though the contrast is less than that for the case presented earlier and the wave envelopes are less organized than those in case 1. Nevertheless, streaks of strong convective peaks are visible on large scales, especially for case 7 in Fig. 11(c1) where groups of such peaks are seen to move eastward at about 2.5 m s^{-1}. Such peaks are seen to move eastward in Fig. 11(a1) at about 2 m s^{-1} for the case 5.

The PDFs in Figs. 11(a2),(a3),(b2),(b3),(c2),(c3), confirm the intuition that convective events of 5 K day^{-1} and stronger are more probable within the warm pool region. However Figs. 11(b3),(c3), corresponding to cases 6 and 7, show PDFs that suggest that, inside the warm pool, 5 K day^{-1} events are at least as probable as events with 3 and 4 K day^{-1}, unlike the PDF in Fig. 11(a3), which decreases monotonically after the classical peak of weak activity at around 1 K day^{-1}.

c. *The extreme cases with $\alpha_c = 2$ and $a_0 = 4$*

The x–t contours of the first baroclinic velocity fluctuations for the last extreme case, in Table 2, with $a_0 = 4$, $a_1 = 0.1$, $a_2 = 0.9$, $\gamma - 2 = 0.05$ (not shown here) reveal three strong moist gravity waves moving westward and circling the globe crossed by a eastward-moving wave with a much stronger amplitude also circling the periodic domain. Those waves do not seem to change much of their strength or propagation speed as they cross the warm pool region but only when they cross each other.

With $a_0 = 4$, in the last case 8 of Table 2, both the climatology and the wave fluctuations become stronger, in agreement with linear theory, which predicts stronger growths with decreasing a_0.

Also as shown on the third row (case 3) of Table 2, when the congestus coefficient in (2.1) is set to $a_c = 2$, the wave fluctuation becomes much stronger. They consist of two giant large-scale gravity waves moving westward at roughly 22 m s^{-1} and circling the globe with deep convective peaks exceeding 60 K day^{-1}.

The climatologies associated with these two cases are shown in Figs. 12a,b. Both these extreme cases deviate considerably from the prototype classical Walker circulation discussed above. They both present some asymmetry in the potential temperature and, to some extent, in the velocity profile. This is clearly a signature of the establishment of a preferred direction of propagation and the structure of the convectively coupled waves in the statistical steady state solutions. Especially, for the case with $\alpha_c = 2$, the temperature is warmer in the lower troposphere, within the warm pool region, which a signature of strong congestus heating rates.

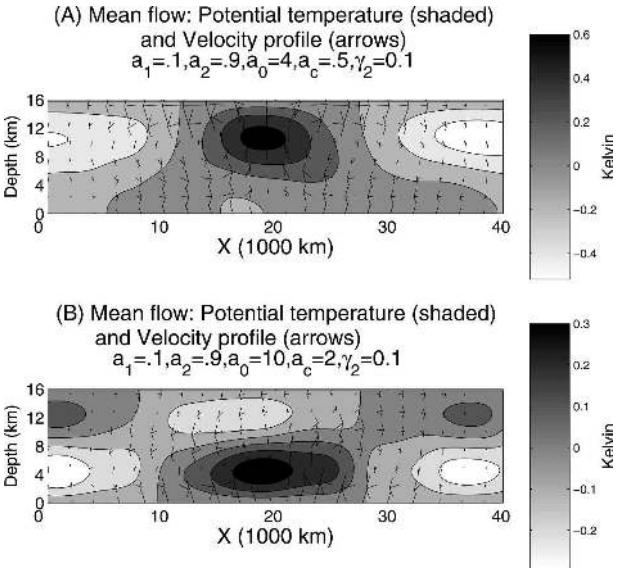

FIG. 12. The x–z structure of the time average flow for the two extreme cases 3 and 8 of Table 2. Potential temperature is shaded and the velocity profile is shown with arrows.

5. Concluding discussion

Nonlinear simulations[3] of convectively coupled waves utilizing the multicloud intermediate parameterization model introduced recently by the authors in (KM06a) are presented here. The model is based on a crude vertical resolution reduced to two vertical baroclinic modes; a deep convective mode and a second mode, which is heated from below by congestus clouds and heated from above by stratiform clouds. Moreover, a switch function is utilized to inhibit or favor deep convection depending on whether the middle troposphere is dry or not. Also the model carries an equation for the vertically averaged water vapor with both first and second baroclinic convergence. A 40 000 km periodic domain, mimicking the equatorial ring without rotation, is assumed, thus reducing the model to a system of partial differential equations in (x, t) plane. The system is forced by an imposed SST with a zonal gradient mimicking the Indonesian warm pool. Starting with initial data consisting of a homogeneous radiative convective equilibrium corresponding to a Jordan sounding, the system is numerically integrated for a period of 800 days, in realistic parameter regimes with a homoge-

[3] Notice nonlinearity is introduced by the use of the nonlinear switch function, Λ, in the deep convection/precipitation and downdrafts formulas, by the use of the Heaviside functions in those formulas, and by the addition of the nonlinear convergence terms on the lhs of the q equation.

neous radiative cooling of 1 K day^{-1}. After a transient period of about 100 to 200 days, the solution reaches a statistical steady state and time averages over the last 500 days were computed. Both the resulting climatology and the wave fluctuations are analyzed and compared for different parameter values.

From the typical simulations in section 3, the statistical steady-state solution is characterized by intermittent and chaotic deep convective events organized within the warm pool region into envelopes of large-scale convectively coupled wave packets with phase speeds between 16 to 20 m s^{-1} and a large-scale group velocity of deep convective organization varying roughly from 2 to 5 m s^{-1}. While an explanation of the 18 to 20 m s^{-1} phase velocity follows naturally from linear theory (KM06a) as corresponding to the basic moist gravity wave instability discussed in that paper, the emergence of the slowly moving envelopes is new and merits more investigation and will be addressed and published elsewhere in the near future. Nevertheless, it is worthwhile mentioning that a closer look and the data revealed that, in some cases, the regions of convective peaks correspond to collusions of convectively coupled gravity waves traveling in opposite directions (see, e.g., Fig. 9, top panel). Deep convective events are also present outside the warm pool region but they are more intermittent, sparse, and much weaker. The time averaged solution depicts a prototype Walker-type climatology with moist and warm air raising from the warm pool in the center of the domain and dry and cold air sinks elsewhere with the descending branch being stronger near the warm pool. The mean potential temperature first and second baroclinic components have a weak gradient with a temperature difference between the warm pool region and the rest of the domain not exceeding 0.5 and 0.2 K, respectively, while the associated total x–z profile shows a second baroclinic feature with a warm upper troposphere above the warm pool, on average. The mean congestus and stratiform heating rates, H_s and H_c, are fairly comparable with H_s largely dominating within the warm pool region so that the mean precipitation/convective heating is maximum in the upper middle troposphere in the center of the domain over the warm pool.

The fluctuations from the Walker-type climatology display mixed deep convective-congestus waves traveling outside and converging toward the warm pool where the deep convection amplifies. The physical structure and dynamical features of these convectively coupled waves are similar to the ones presented and documented in KM06a and Khouider and Majda (2006b), qualitatively resembling the observed convectively coupled tropical Kelvin waves (Straub and Kiladis 2002; Majda et al. 2004). The role of congestus cloudiness and second baroclinic convergence during the moistening and preconditioning episode, which are well documented in Khouider and Majda (2006b), are also evident here. However, with the realistic radiative cooling of 1 K day^{-1}, the CAPE regeneration episode starts with the decrease of the dry static stability, $\theta_1 + \gamma_2\theta_2$, then it is followed by the raising of θ_{eb}. Consequently, as in the simulations with the weak radiative cooling in Khouider and Majda (2006b), the value of the convective buoyancy frequency, a_0, is crucial here for both the strength of the wave fluctuations and the intermittency of deep convective events. Large values such as $a_0 = 20$ make the Walker cell stable with no wave fluctuations while too-small values such as $a_0 = 4$ lead to nonphysically large waves moving around the periodic domain (globe) without a classical Walker cell.

Moreover, variation of other model parameters with a reasonably small decrease of a_0 to $a_0 = 7.5$ in section 4, changes mainly the organization of the convective events but does not affect the climatology very much. Nevertheless, it is worthwhile mentioning that all the cases considered herein and listed in Tables 1 and 2, have small growths from linear theory (KM06a) of about 0.5 K day^{-1} except for the cases with $a_0 = 4$ and $\alpha_c = 2$, which have growths exceeding 1.5 K day^{-1} and the case $a_0 = 20$, which is linearly stable. Therefore, as one would expect the realistic parameter regimes for the multicloud simulations are among the parameter values for which linear theory predicts reasonably small growth rates of about 0.5 K day^{-1} so linear theory is a useful rough guideline.

The success of the present simulations utilizing an appropriate intermediate model parameterization with only two vertical modes but carrying all the three cloud types, congestus, stratiform, and deep convective, and implicitly including nonprecipitating boundary layer clouds, in qualitatively reproducing the large-scale features of organized tropical convection almost as seen in cloud-resolving modeling simulations (Grabowski et al. 2000; Grabowski and Moncrieff 2001; Grabowski 2001, 2003) is not surprising; there is increasing observational evidence for the dynamic role of two baroclinic modes in tropical convective dynamics (Lin and Johnson 1996; Johnson et al. 1999; Straub and Kiladis 2002; Haertel and Kiladis 2004; Kiladis et al. 2005). Also a more recent study by Peters and Bretherton (2006) of CRM data revealed that the first and second baroclinic vertical modes carry about 99% of the convective variability.

The 2D multicloud simulations presented in this paper are not intended specifically as a model for the MJO but to elucidate some aspects of organized tropi-

cal convection and convectively coupled waves. Although, in the nonlinear simulations presented here, we see large-scale organization of convection, we do not believe/claim that this is an MJO per se. Here gravity wave activity and wave interaction and their effect on large-scale organization are exaggerated because of the lack of rotation and meridional dependence. Numerical simulations using the multicloud parameterization on an equatorial beta plane are in progress and will be reported in the near future by the authors. Also a future version of the multicloud parameterizations will carry an active radiation scheme including the wind shear effects on anvil clouds (Lin and Mapes 2004).

Acknowledgments. The research of B.K. is supported by a University of Victoria startup grant and a grant from the Natural Sciences and Engineering Research Council of Canada. The research of A.M. is partially supported by ONR N0014-96-1-0043, NSF DMS-0456713, and NSF-FRG DMS-0139918. The authors are thankful to M.W. Moncrieff for sponsoring a visit for B.K. to NCAR during the summer of year 2004 where this work was partly initiated.

REFERENCES

Bretherton, C. B., and A. H. Sobel, 2002: A simple model of a convectively coupled Walker circulation using the weak temperature gradient approximation. *J. Climate,* **15,** 2907–2920.

——, M. E. Peters, and L. E. Back, 2004: Relationship between water vapor path and precipitation over the tropical oceans. *J. Climate,* **17,** 1517–1528.

Charney, J. G., and A. Eliassen, 1964: On the growth of the hurricane depression. *J. Atmos. Sci.,* **21,** 68–75.

Craig, G. C., and S. L. Gray, 1996: CISK or WISHE as the mechanism for tropical cyclone intensification. *J. Atmos. Sci.,* **53,** 3528–3540.

Dunkerton, T. J., and F. X. Crum, 1995: Eastward propagating 2- to 15-day equatorial convection and its relation to the tropical intraseasonal oscillation. *J. Geophys. Res.,* **100,** 25 781–25 790.

Emanuel, K. A., 1987: An air–sea interaction model of intraseasonal oscillations in the tropics. *J. Atmos. Sci.,* **44,** 2324–3240.

——, J. D. Neelin, and C. S. Bretherton, 1994: On large-scale circulations in convecting atmosphere. *Quart. J. Roy. Meteor. Soc.,* **120,** 1111–1143.

Fuchs, Z., and D. Raymond, 2002: Large-scale modes of a nonrotating atmosphere with water vapor and cloud-radiation feedbacks. *J. Atmos. Sci.,* **59,** 1669–1679.

Gill, A. E., 1982: *Atmosphere–Ocean Dynamics.* Academic Press, 666 pp.

Grabowski, W. W., 2001: Coupling cloud processes with large-scale dynamics using the Cloud-Resolving Convection Parameterization (CRCP). *J. Atmos. Sci.,* **58,** 978–997.

——, 2003: MJO-like coherent structures: Sensitivity simulations using the Cloud-Resolving Convection Parameterization (CRCP). *J. Atmos. Sci.,* **60,** 847–864.

——, and M. W. Moncrieff, 2001: Large-scale organization of tropical convection in two dimensional explicit numerical simulations. *Quart. J. Roy. Meteor. Soc.,* **127,** 445–468.

——, J.-I. Yano, and M. W. Moncrieff, 2000: Cloud-resolving modeling of tropical circulations driven by large-scale SST gradients. *J. Atmos. Sci.,* **57,** 2022–2039.

Haertel, P. T., and G. N. Kiladis, 2004: On the dynamics of two-day equatorial disturbances. *J. Atmos. Sci.,* **61,** 2707–2721.

Johnson, R. H., T. M. Rickenbach, S. A. Rutledge, P. E. Ciesielski, and W. H. Schubert, 1999: Trimodal characteristics of tropical convection. *J. Climate,* **12,** 2397–2407.

Khouider, B., and A. J. Majda, 2005a: A non-oscillatory well balanced scheme for an idealized tropical climate model. Part I: Algorithm and validation. *Theor. Comp. Fluid. Dyn.,* **19,** 331–354.

——, and ——, 2005b: A non-oscillatory well balanced scheme for an idealized tropical climate model. Part II: Nonlinear coupling and moisture effects. *Theor. Comp. Fluid Dyn.,* **19,** 355–375.

——, and ——, 2006a: A simple multicloud parameterization for convectively coupled tropical waves. Part I: Linear analysis. *J. Atmos. Sci.,* **63,** 1318–1323.

——, and ——, 2006b: Model multicloud parameterizations for convectively coupled waves: Detailed nonlinear wave evolution. *Dyn. Atmos. Oceans,* **42,** 59–80.

Kiladis, G. N., K. H. Straub, and P. Haertel, 2005: Zonal and vertical structure of the Madden–Julian oscillation. *J. Atmos. Sci.,* **62,** 2790–2809.

Lin, J.-L., and B. Mapes, 2004: Wind shear effects on cloud-radiation feedback in the western Pacific warm pool. *Geophys. Res. Lett.,* **31,** L16118, doi:10.1029/2004GL020199.

Lin, X., and R. H. Johnson, 1996: Kinematic and thermodynamic characteristics of the flow over the Western Pacific Warm Pool during TOGA COARE. *J. Atmos. Sci.,* **53,** 695–715.

Lindzen, R. S., 1974: Wave–CISK in the Tropics. *J. Atmos. Sci.,* **31,** 156–179.

Majda, A. J., and M. Shefter, 2001: Models for stratiform instability and convectively coupled waves. *J. Atmos. Sci.,* **58,** 1567–1584.

——, and B. Khouider, 2002: Stochastic and mesoscopic models for tropical convection. *Proc. Natl. Acad. Sci. USA,* **99,** 1123–1128.

——, ——, G. N. Kiladis, K. H. Straub, and M. G. Shefter, 2004: A model for convectively coupled tropical waves: Nonlinearity, rotation, and comparison with observations. *J. Atmos. Sci.,* **61,** 2188–2205.

Mapes, B. E., 2000: Convective inhibition, subgrid-scale triggering energy, and "stratiform instability" in a toy tropical wave model. *J. Atmos. Sci.,* **57,** 1515–1535.

Moncrieff, M. W., and E. Klinker, 1997: Organized convective systems in the tropical western Pacific as a process in general circulation models: A TOGA-COARE case study. *Quart. J. Roy. Meteor. Soc.,* **123,** 805–827.

Nakazawa, T., 1988: Tropical super clusters within intraseasonal variations over the western Pacific. *J. Meteor. Soc. Japan,* **66,** 823–839.

Neelin, J. D., and J. Yu, 1994: Modes of tropical variability under convective adjustment and Madden–Julian oscillation. Part I: Analytical theory. *J. Atmos. Sci.,* **51,** 1876–1894.

——, and N. Zeng, 2000: A quasi-equilibrium tropical circulation model—Formulation. *J. Atmos. Sci.,* **57,** 1741–1766.

Peters, M. E., and C. S. Bretherton, 2006: Structure of tropical variability from a vertical mode perspective. *Theor. Comp. Fluid Dyn.,* **20,** 501–524.

Slingo, J. M., and Coauthors, 1996: Intraseasonal oscillation in 15 atmospheric general circulation models: Results from an AMIP diagnostic subproject. *Climate Dyn.,* **12,** 325–357.

Sperber, K. R., J. M. Slingo, P. K. Inness, and W. K.-M. Lau, 1997: On the maintenance and initiation of the intraseasonal oscillation in the NCEP/NCAR reanalysis and in the GLA and UKMO AMIP simulations. *Climate Dyn.,* **13,** 769–795.

Straub, K. H., and G. N. Kiladis, 2002: Observations of a convectively-coupled Kelvin wave in the eastern Pacific ITCZ. *J. Atmos. Sci.,* **59,** 30–53.

Tompkins, A. M., 2001a: Organization of tropical convection in low vertical wind shears: The role of water vapor. *J. Atmos. Sci.,* **58,** 349–364.

——, 2001b: On the relationship between tropical convection and sea surface temperature. *J. Climate,* **14,** 633–637.

Tulich, S. N., D. A. Randall, and B. E. Mapes, 2007: Vertical-mode and cloud decomposition of large-scale convectively coupled gravity waves in a two dimensional cloud-resolving model. *J. Atmos. Sci.,* in press.

Wheeler, M., and G. N. Kiladis, 1999: Convectively coupled equatorial waves: Analysis of clouds and temperature in the wavenumber-frequency domain. *J. Atmos. Sci.,* **56,** 374–399.

——, ——, and P. J. Webster, 2000: Large-scale dynamical fields associated with convectively coupled equatorial waves. *J. Atmos. Sci.,* **57,** 613–640.

Yano, J.-I., and K. A. Emanuel, 1991: An improved model of the equatorial troposphere and its coupling to the stratosphere. *J. Atmos. Sci.,* **48,** 377–389.

——, J. C. McWilliams, M. W. Moncrieff, and K. A. Emanuel, 1995: Hierarchical tropical cloud systems in an analog shallow-water model. *J. Atmos. Sci.,* **52,** 1723–1742.

Zehnder, J. A., 2001: A comparison of convergence- and surface-flux-based convective parameterizations with applications to tropical cyclogenesis. *J. Atmos. Sci.,* **58,** 283–301.

Zhang, C., 2005: Madden-Julian Oscillation. *Rev. Geophys.,* **43,** RG2003, doi:10.1029/2004RG000158.